The Effect of Eurasian Snow Cover on the Indian Monsoon

A. D. VERNEKAR AND J. ZHOU

Department of Meteorology, University of Maryland, College Park, Maryland

J. SHUKLA

Center for Ocean-Land-Atmosphere Studies, Calverton, Maryland

(Manuscript received 15 November 1993, in final form 1 July 1994)

ABSTRACT

The authors successfully model and simulate the observed evidence that anomalously high winter/spring Eurasian snow cover is linked to weak rainfall in the following summer Indian monsoon. It is shown that excessive snow cover in February reduces June to September precipitation over India. The excessive snow cover is associated with a weak monsoon characterized by higher sea level pressure over India, a weaker Somali jet, weaker lower tropospheric westerlies, and weaker upper tropospheric easterlies. The weak monsoon is also associated with weaker secondary circulations. The remote response to excessive Eurasian snow cover is to reduce the strength of trade winds in the eastern equatorial Pacific Ocean. Energy used in melting excessive snow reduces the surface temperature over a broad region centered around the Tibetan Plateau. Reduced surface sensible heat flux reduces the midtropospheric temperature over the Tibetan Plateau. The result is to reduce the midtropospheric meridional temperature gradient over the Indian peninsula, which weakens the monsoon circulation.

1. Introduction

More than a century ago, Blanford (1884) suggested the inverse relation between Himalayan winter and spring snow accumulation and subsequent summer monsoon rainfall over India. This relation was later substantiated with additional data by Walker (1910). Because of an inadequate observational network to obtain the spatial variation of snow cover over the Himalayan region, little progress was made until the availability of satellite measurements. Hahn and Shukla (1976) used snow cover data derived from satellite observations to show that the correlation between winter Eurasian snow cover south of 52°N and the following Indian summer monsoon rainfall is negative and statistically significant. This result was further supported by Dey and Bhanu Kumar (1982, 1983) and Dickson (1984). The relationship between snow cover and monsoon circulation is consistent with a suggestion by Charney and Shukla (1981) that the Indian monsoon circulation is a dynamically stable system and its interannual variations are largely determined by slowly varying surface boundary conditions.

The monsoon circulation is characterized by a reversal of the zonal mean annual mean midtropospheric temperature gradient between the equator and 30°N. That is, during the summer monsoon, the equator is colder than northern India. A weaker meridional temperature gradient between the equator and 30°N can delay and weaken the monsoon circulation. Shukla (1987) hypothesized that an excessive snowfall during the previous winter and spring seasons can delay the build up of the monsoonal temperature gradient because part of the solar energy will be reflected and part will be utilized for melting the snow or for evaporating the soil moisture. A relatively small amount of energy will be left for warming the surface and hence the atmosphere.

Recently, three general circulation model (GCM) studies (Barnett et al. 1989; Yasunari et al. 1991; Zwiers 1993) reported on experiments to investigate the physical mechanisms responsible for the relation between Eurasian snow cover and the Asian summer monsoon. Barnett et al. (1989) used the European Centre for Medium Range Weather Forecasts (ECMWF) spectral model with triangular truncation at wavenumber 21 and 16 levels in the vertical. They investigated the influence of snow melting and evaporation as well as the snow albedo effect from experiments with different snowfall rates. They found that the effect of albedo alone was not significant but that the effect of snow melting and evaporation in addition to the albedo effect significantly diminished the intensity of Asian summer monsoon circulations. Yasunari et al. (1991) used the Meteorological Research Institute gridpoint GCM with

Corresponding author address: Prof. A. D. Vernekar, Department of Meteorology, University of Maryland, College Park, MD 20742-2425.

horizontal resolution of 4° lat × 5° long and five levels in the vertical. In their anomaly experiment, they added 5-cm water equivalent snow cover depth over Eurasia between 30°–60°N on 1 March to the snow cover in the control experiment. They found that the albedo effect dominates in the spring to reduce the surface temperature, particularly over Tibet. However, in summer, increased evaporation of excess water due to snowmelt cools the surface, especially in the middle latitudes. In the anomaly experiment, the Asian monsoon circulations were weaker and precipitation reduced up to 20% over southeast Asia compared to that of the control run. Zwiers (1993) used the Canadian Climate Centre's spectral GCM with triangular truncation at 20 waves and 10 levels in the vertical. He analyzed the data over Asia from two long integrations with the model, one for 38 years and another for 20 years. He argued that an excess of snow cover over Tibet (or Eurasia) reduces the surface sensible heat flux and that the reduction occurs during the Asian monsoon rainy season. He computed the canonical correlations between surface sensible heat flux over Tibet (and over Eurasia) and precipitation over southeast Asia for June, July, and August (JJA). He found a positive correlation between Tibetan sensible heat flux and southeast Asian rainfall suggesting an inverse relationship between Tibetan snow cover and southeast Asian rainfall. Similar results were obtained when Tibetan and Eurasian surface sensible heat fluxes were considered, implying that it is the Tibetan snow cover rather than the Eurasian snow cover that influences the monsoon circulation.

All three studies were based on models with low horizontal resolution. The models were able to simulate large-scale features of the Asian monsoon but they had deficiencies in simulating regional features of the Indian monsoon, particularly the precipitation pattern. The results of these studies show that the Eurasian snow cover reduces the intensity of the Asian monsoon. Most of the known empirical evidence is between Eurasian snow cover and the Indian monsoon and not the whole Asian monsoon (including southeast Asian and east Asian monsoons). The relation between Eurasian snow cover and the Chinese monsoon is rather complicated. Recently, Yang and Xu (1994) divided China into five regions having similar characteristics of interannual rainfall variability. They correlated JJA rainfall of each one of these regions and Eurasian snow cover. They found that out of five regions, two are positively correlated while three are negatively correlated. The purpose of the present study is to investigate the Eurasian snow cover and Indian summer rainfall connection with the aid of a GCM with relatively higher resolution and that is able to simulate the main regional features of the Indian monsoon. Section 2 describes the experimental design. The results are presented in section 3. A discussion and concluding remarks are given in section 4.

2. Experiment design

We conducted two experiments with the Center for Ocean–Land–Atmosphere Studies (COLA) GCM. In this section we describe the model, snow cover data, and the experiment.

a. The model

The COLA GCM is a spectral model with rhomboidal truncation with 40 waves and 18 levels in the vertical. The dynamics of the model are based on the primitive equations. Large-scale orographic effects are simulated by a modified mean orography computed on the model Gaussian grid ($\approx$1.76°lat × 2.81°long) from the U.S. Navy 10-min elevation data. The modifications are to reduce the amplitude of Gibbs oscillations in a truncated spectral transform (Zhou 1993; Fennessy et al. 1994). Surface wave drag and the vertical distribution of wave drag due to vertically propagating gravity waves induced by subgrid-scale orography are parameterized following procedures by Pierrehumbert (1987), Palmer et al. (1986), and Helfand et al. (1987) (see Vernekar et al. 1992; Kirtman et al. 1993). Exchange of momentum, heat, and water vapor between the earth's surface and the atmosphere are simulated with a simplified biosphere model (Xue et al. 1991, after Sellers et al. 1986). The parameterization of the surface layer is based on the Monin–Obukhov similarity theory. Planetary boundary layer processes are parameterized using the Mellor–Yamada level 2 turbulent closure scheme (1982). The model includes the diurnal cycle. Shallow convection is parameterized following Tiedtke (1984). Deep convection is parameterized using the Kuo (1965) scheme modified by Anthes (1977). Parameterization of longwave radiation is based on Harshvardhan et al. (1987) and that of shortwave radiation follows Lacis and Hansen (1974). Interaction between radiation and model-generated supersaturation and cumulus clouds is based on the scheme of Slingo (1980) and Slingo (1987) (see Hou 1990). Precipitation is due to large-scale supersaturation and subgrid-scale moist convection. If the surface temperature is less than the freezing point of water, the precipitation is taken to be snow. Snow accumulates on the ground and on the canopy. The depth of snow intercepted on the ground is five times the equivalent of liquid water. Snow melts when the surface temperature exceeds 273 K. Snow cover influences radiation, turbulent transfer processes, and the heat capacity of the canopy. When snow melts, soil moisture and runoff are affected. Soil moisture and snow cover are prescribed from climatology initially but subsequently predicted by the model. Daily variations of sea surface temperature (interpolated from monthly mean data) are prescribed. Also, the seasonal variation of vegetation cover is prescribed.

The model simulates the Indian monsoon circulations fairly accurately. Here we show some of the results

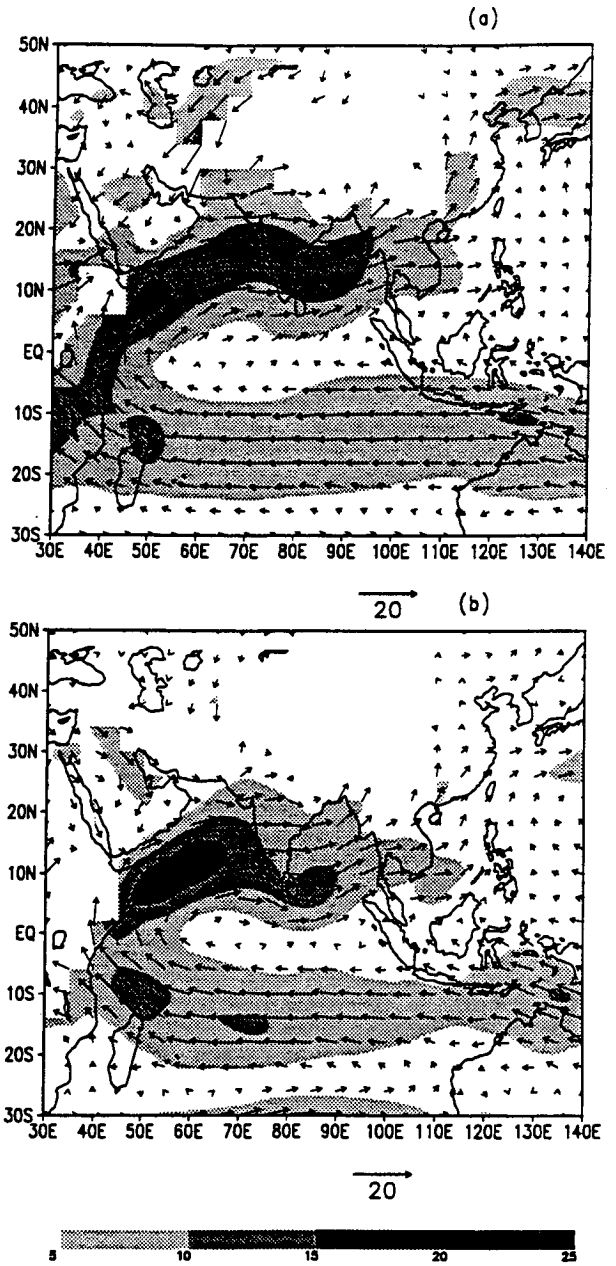

FIG. 1. Regional distribution of 1988 JJA 850-mb wind (m s^{-1}). (a) Model simulation. (b) NMC analysis. Lower scale of gray shade shows magnitude of wind.

of 1988 summer monsoon simulations. The model was integrated from 2 June to 30 August using 2 June 1988 initial conditions and prescribing the seasonal variation of 1988 sea surface temperature. Figure 1 shows a comparison of simulated JJA 850-mb winds and corresponding NMC analysis for 1988. The flow pattern showing easterly wind over the southern Indian Ocean, the Somali Jet, southwesterly flow over the Arabian Sea, westerly flow over the Indian peninsula, and the southwesterly flow over the Bay of Bengal agrees well with the NMC analysis. Even the strength of the Somali Jet and the westerly flow over the peninsula are in good agreement with those of the NMC analysis. The simulated 200-mb circulation and the corresponding NMC analysis are shown in Fig. 2. The simulated circulations associated with the Tibetan High, the equatorial easterly jet of ~25 m s^{-1} and the westerly jet north of Tibet of ~30 m s^{-1} agree well with the analysis. The real test of a model is in its ability to simulate the amplitude and phase of the precipitation pattern. Figure 3 shows a comparison between the simulated precip-

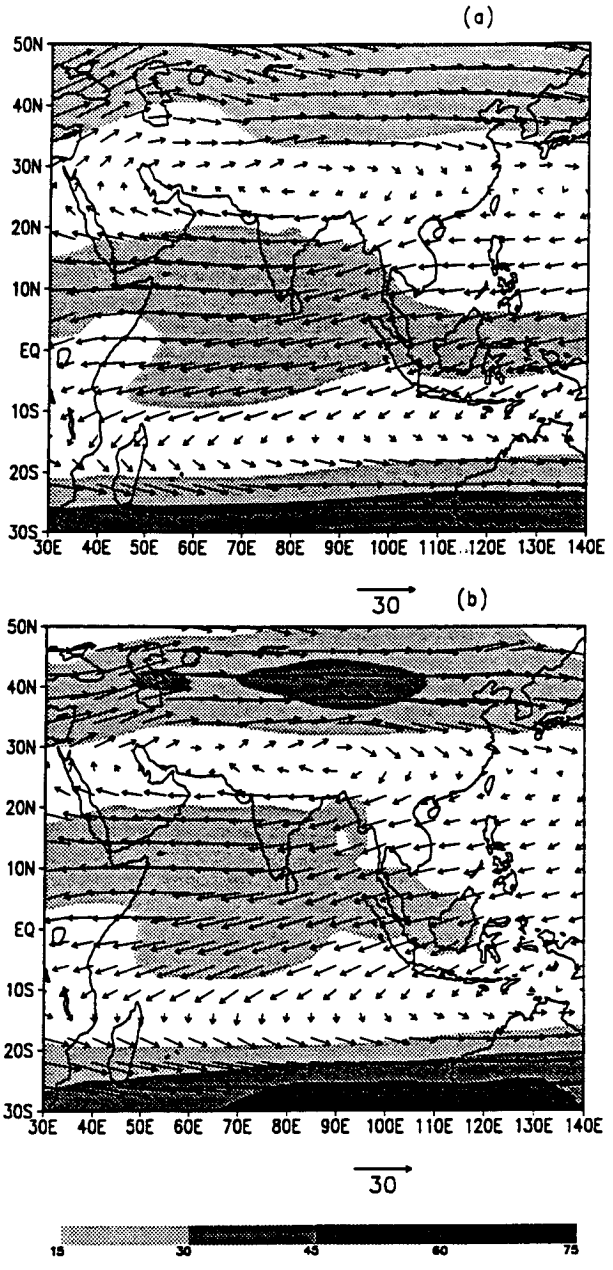

FIG. 2. Same as Fig. 1 but for 200 mb.

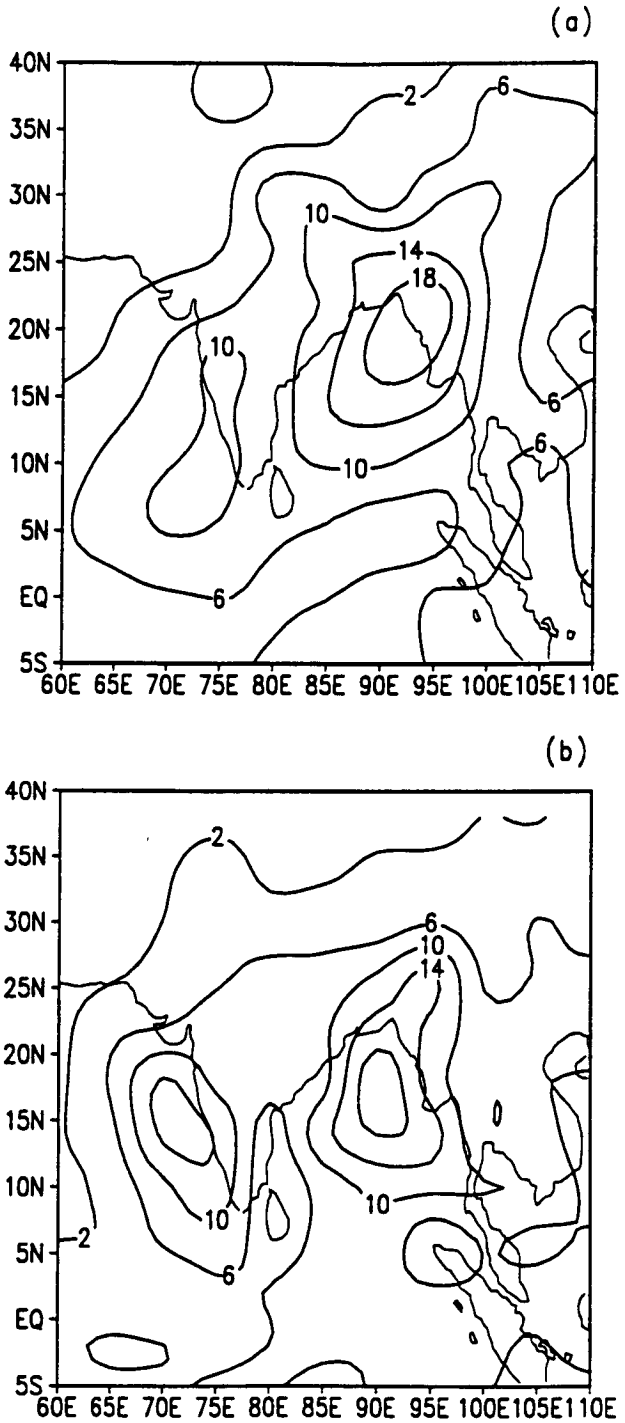

FIG. 3. Regional distribution of 1988 JJA precipitation rate (a) Model simulation. (b) Observations (see text). Contour interval is 4 mm day^{-1}.

itation pattern and the precipitation derived from observed data. The observed data are a combination of gridded station data over land (Global Precipitation Climatology Project, Janowiak and Arkin 1991) and precipitation derived from the Microwave Sounding Unit satellite data over the ocean (Spencer 1993). The precipitation pattern and its magnitude in eastern India are accurately simulated. However, the magnitude of precipitation near the western Ghats (a low mountain range along the western side of the Indian peninsula) is underestimated. Otherwise the general features are in agreement with the observations.

b. Snow cover data and experiments

Empirical studies mentioned in the introduction, in particular, Hahn and Shukla (1976), show an inverse relationship between winter (DJFM) Eurasian snow cover extent and the following summer (JJAS) rainfall over India. Climatological seasonal variation of Eurasian snow cover shows that the maximum snow cover extent occurs in February (Matson et al. 1986). Therefore, we started the model integration from February. To prescribe the initial snow cover anomaly, we need a measure of the geographical distribution of interannual variability of snow extent and snow depth. Accurate estimates of snow extent are available for several years from weekly digitized maps analyzed and archived by the National Environmental Satellite Data and Information Service, NOAA, but the snow depth information is not available. Schutz and Bregman (1988) provide monthly mean climatology snow extent and depth derived from surface station observations but no information on interannual variability. There are several datasets from surface station data with interannual variability but these observations are not representative of variability on a continental scale.

The only global dataset available on interannual variability of snow depth is from the *Nimbus-7* Scanning Multichannel Microwave Radiometer (SMMR). These data are derived by utilizing the scattering properties of microwaves emerging from the earth's surface. In the dry snowpack, snow crystals scatter and redistribute the microwave radiation emerging from the underlying soil. At 37 GHz, the scattering coefficient of snow is much larger than the absorption coefficient, whereas at 18 GHz, absorption becomes the dominant effect. There is a general increase in the scattering of microwave energy with increasing snow depth leading to a lower microwave brightness temperature. Chang et al. (1987) have shown that snow depth can be estimated from a relationship that depends on the difference between passive microwave brightness temperature in the 18- and 37-GHz channels. The accuracy of these estimates deteriorates if there is wet snow. The relationship fails when snow depth is less than 2 cm. In spite of these problems, the monthly mean climatology based on nine years of data (1979–1987) compares favorably with the climatology compiled by Schutz and Bregman (1988). From the nine years of data, we computed the anomaly in snow depth for January and February data, and we linearly interpolated

in time to obtain the maximum and minimum snow depth for February 1, 2, 3, and 4. From here onward we shall use "heavy" snow cover for the maximum snow depth and "light" snow cover for the minimum snow depth. The distribution of heavy snow cover over Eurasia for 2 February is shown in Fig. 4a. Snow depth is shown in mm water equivalent. The 50-mm water equivalent isoline covers a large fraction of Eurasia. Snow cover larger than 100-mm water equivalent is largely in Siberia and a relatively small region over eastern Tibet. The snow depth distribution for 2 February light snow is shown in Fig. 4b. In this case, the 50-mm water equivalent isoline very nearly covers the region covered by 100-mm water equivalent in Fig. 4a. In the light snow cover, Tibet is covered with less than 25-mm water equivalent. The difference between heavy and light snow depth is shown in Fig. 4c. The largest differences are over eastern Tibet, Mongolia, and Siberia. Most of the difference is about 50-mm water equivalent. The magnitude of the difference is comparable to the anomaly prescribed by Yasunari et al. (1991) in a similar experiment.

Two experiments were made by integrating the model in an annual cycle mode from the beginning of February to the end of September. In one experiment we initially prescribe the heavy snow cover over Eurasia and in the other experiment, the light snow cover. From here onward, we shall refer to the experiment with initial heavy snow cover as HSE and that with the light snow cover, LSE. The initial snow cover over the rest of the globe was prescribed from climatology based on nine years of data. The SST, soil moisture, and vegetation cover were prescribed from climatology. The SST data were obtained from Reynolds (1988), the soil moisture data from Mintz and Serafini (1984), and the vegetation cover from Dorman and Sellers (1989). For each experiment, we made four runs with atmospheric initial conditions for four consecutive days. The four initial atmospheric conditions were for 0000 UTC 1–4 February 1986 from NMC analysis. We have used the initial Eurasian snow cover anomalies for the corresponding days derived from the SMMR data. The results of these two experiments are presented in the next section.

3. Results

All the results presented here are based on ensemble means of four realizations, with initial conditions of

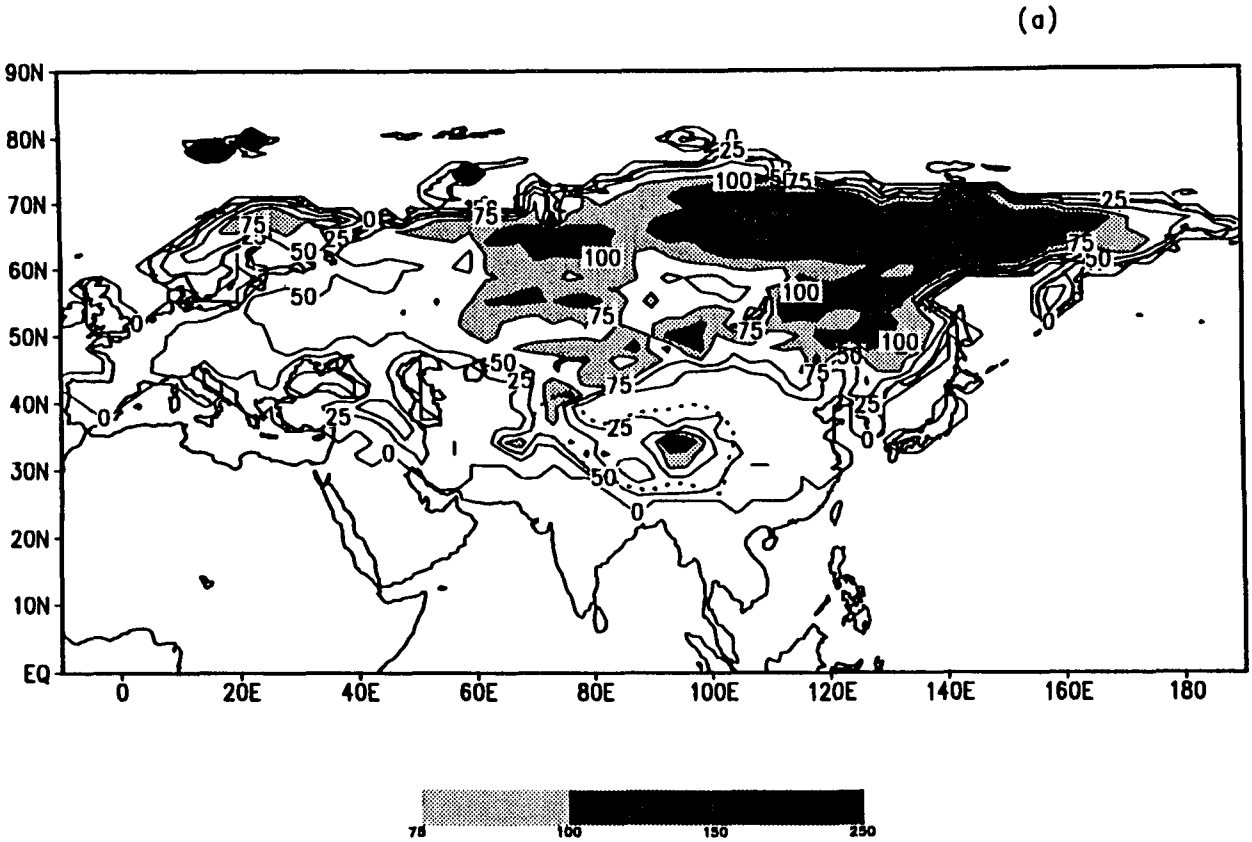

FIG. 4. Initial snow cover distribution over Eurasia for 2 February. (a) For heavy snow cover experiment (HSE). (b) For light snow cover experiment (LSE). (c) Initial snow cover difference (HSE − LSE). Contour interval is 25-mm water equivalent. Dotted curve shows 2.5-km model orography contour surrounding the Tibetan Plateau.

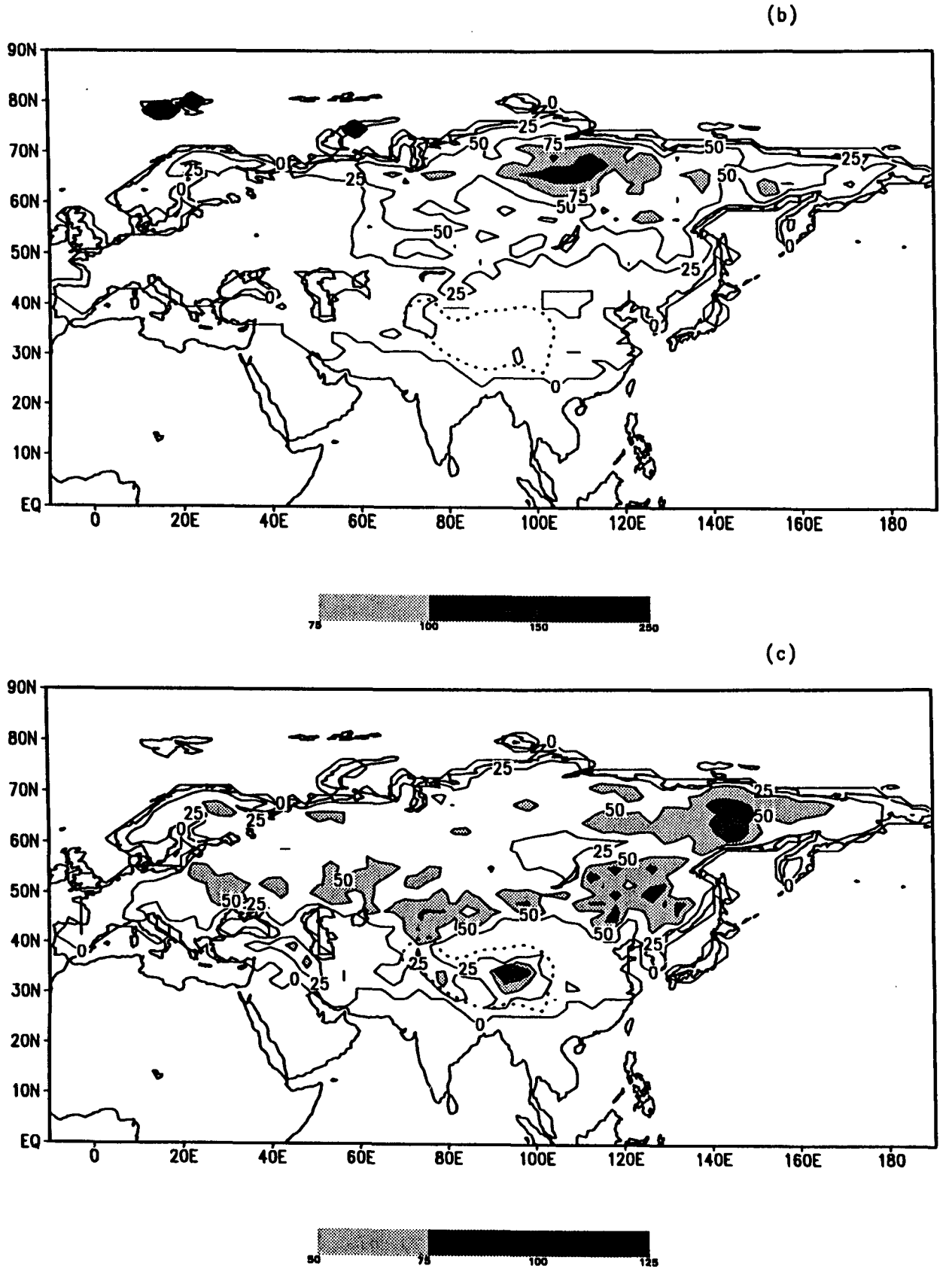

FIG. 4. (*Continued*)

1–4 February 1986 for each experiment. As mentioned earlier, the model predicts snow accumulation and snow melting during integration. The seasonal variation of snow extent over Eurasia is similar in both of the experiments (see Fig. 5). The initial extent of Eurasian snow cover is ~30 million square kilometers in HSE and ~26 million square kilometers in LSE. The snow extent generally decreases as the warm season progresses. It starts accumulating slowly from mid-September. These characteristics of snow extent variations agree well with the observations (see, e.g., Matson et al. 1986). The major difference in the two experiments is in the initial value and the seasonal variation of snow depth. The initial snow depth in the HSE is almost twice as much as in the LSE (see Fig. 6). In both of the experiments, the snow depth increases in early spring and then starts decreasing in early May. Most of the snow is melted by the end of June. These snow depth variations are similar to those in the observations (Schutz and Bregman 1988). The rate at which the snow is melted differs in the two experiments, especially in May and June. Snowmelt rate in HSE during this period is higher than that in the LSE.

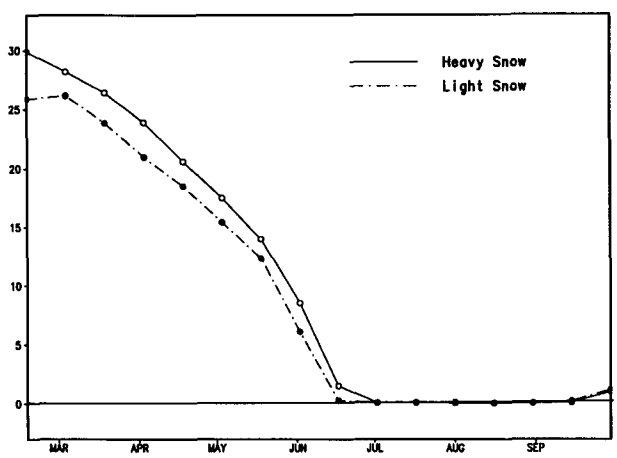

FIG. 5. Seasonal variation of snow cover extent over Eurasia (10^6 km^2) in the model. Tick marks on the abscissa refer to the beginning of the month.

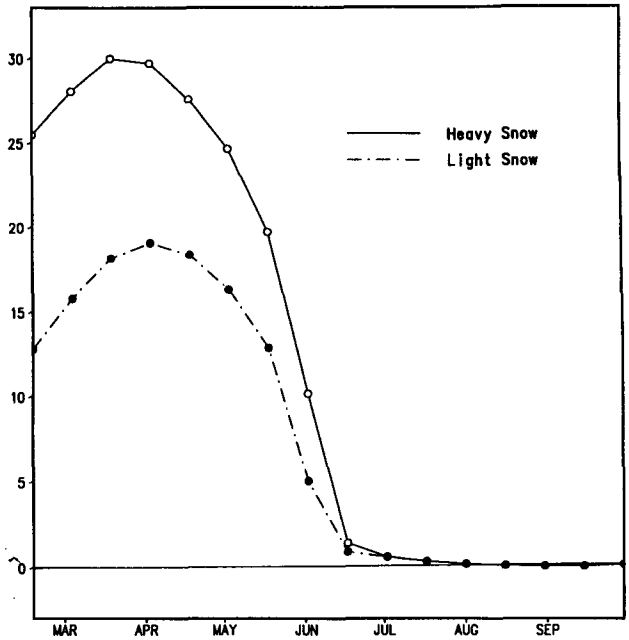

FIG. 6. Seasonal variation of total snow mass over Eurasia (10^{14} kg water equivalent) in the model. Tick marks on the abscissa refer to the beginning of the month.

a. Thermal effects of the Tibetan Plateau

One of the conditions for the establishment of the summer monsoon is the reversal of midtropospheric meridional temperature gradient between the equator and 30°N along the Indian peninsula. The intensity of the monsoon circulation to a large extent is proportional to the magnitude of the temperature gradient. For the reversal of the temperature gradient, the midtropospheric temperature around 30°N has to be warmer than that at the equator. Several studies have been made to determine the mechanisms of pre-monsoonal heating. Flohn (1950, 1960) was the first to suggest that the Tibetan massif heats the midtroposphere largely by the surface sensible heat flux because of its average elevation of 4 km. Riehl (1959) showed that heavy rainfall in eastern Tibet, Assam, and Burma in late April and May contributes to the midtropospheric heating due to the latent heat of condensation. Later studies (Yeh 1981; Gao et al. 1981) based on surface and upper-air observations over Tibet suggest that the ratio of sensible heat flux to the latent heat flux is close to two while there were large differences between the western and eastern Tibetan Plateau. Recent studies based on the FGGE data by Nitta (1983), Luo and Yanai (1984), He et al. (1987), and Yanai and Li (1994) showed results supporting Flohn's hypothesis that the Tibetan Plateau acts as an elevated heat source [see Yanai et al. (1992) for review]. From two general circulation model experiments, one with and one without mountains, Hahn and Manabe (1975) clearly demonstrated that the presence of mountains in general and that of the Tibetan Plateau in particular is essential in establishing and maintaining the Indian summer monsoon. Kuo and Qian (1981, 1982) have simulated the July monsoon with a numerical model that includes the effects of the diurnal cycle. They made several experiments including one with and one without mountains to show that mountains (Tibetan Plateau) and diurnal variations are essential to simulate realistic precipitation patterns.

The May 500-mb temperature difference (HSE − LSE) shows a negative region centered over the Tibetan Plateau (see Fig. 7). The maximum cooling of

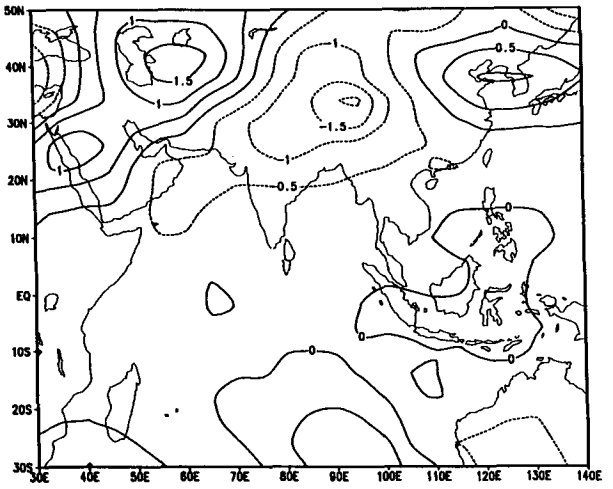

FIG. 7. Regional distribution of May 500-mb temperature difference (HSE − LSE). Contour interval is 0.5 K.

2 K is over the region of maximum initial snow cover difference between the two experiments (Fig. 4c) suggesting a direct influence of initial snow cover. To study the role of snow cover on the heating processes in the atmospheric column over this region, we examined the surface heat fluxes and components of diabatic heating in the atmosphere over a region surrounding the Tibetan Plateau. For time average conditions (averaging time one month), the surface energy balance can be written following Peixoto and Oort (1992) as

$$F_{\text{rad}} - F^{\uparrow}_{\text{SH}} - F^{\uparrow}_{\text{LH}} - F^{\downarrow}_{G} - F_{M} = 0, \qquad (1)$$

where $F_{\text{rad}} = F^{\downarrow}_{S}(1 - \alpha_S) - \epsilon\sigma T_S^4 + F^{\downarrow}_{\text{LW}}$, net radiative heating

$F^{\downarrow}_{S}$—solar radiation reaching the earth's surface
α_S—albedo of the earth's surface
ϵ—thermal emissivity of the earth's surface
σ—Stefan–Boltzmann constant
T_S—surface (ground) temperature
$F^{\downarrow}_{\text{LW}}$—atmospheric radiation arriving at the earth's surface
$F^{\uparrow}_{\text{SH}}$—upward sensible heat flux
$F^{\uparrow}_{\text{LH}}$—latent heat flux due to phase change of water (liquid to vapor)
$F^{\downarrow}_{G}$—downward sensible heat flux to subsurface layers due to diffusion
F_M—latent heat energy used to melt snow (or ice).

When snow is present on the ground, $\alpha_S = 0.8$ but it is reduced to 0.48 when $T_S \approx 273$ K to account for puddles of water. When all the snow is melted, α_s is determined by the biosphere model (Sellers et al. 1986) depending on the vegetation cover. The thermal emissivity, ϵ, of snow is higher than most other surface covers. As a result, it tends to increase infrared radiation emitted. Snow acts as a thermal insulator because of its low thermal conductivity. Snow melting (water freezing) is a sink (source) for latent heat. When snow melts water is available for evaporation, runoff, and to increase the soil moisture by diffusion and gravitational transport.

The three panels (a, b, and c) of Fig. 8 show the seasonal variation of the difference (HSE − LSE) of surface heat fluxes, snowmelt, and surface temperature areally averaged over the region (28°–40°N, 70°–105°E), respectively. The middle panel (Fig. 8b) shows there is no difference in snowmelt over the region in February and March. Snowmelt is larger in HSE than in LSE in April–July with a maximum difference of ~10-mm water equivalent in May. The surface temperature difference (HSE − LSE) shown in Fig. 8c is negative from February to August with a minimum of −0.9°K in May when the snowmelt difference is maximum. The positive (negative) values of the surface heat fluxes in Fig. 8a indicate that fluxes are converging (diverging) at (from) the surface to increase (decrease) the surface temperature in HSE. By Eq. (1), the sum of the heat flux differences must be zero for every month. The difference in the heat fluxes are large as

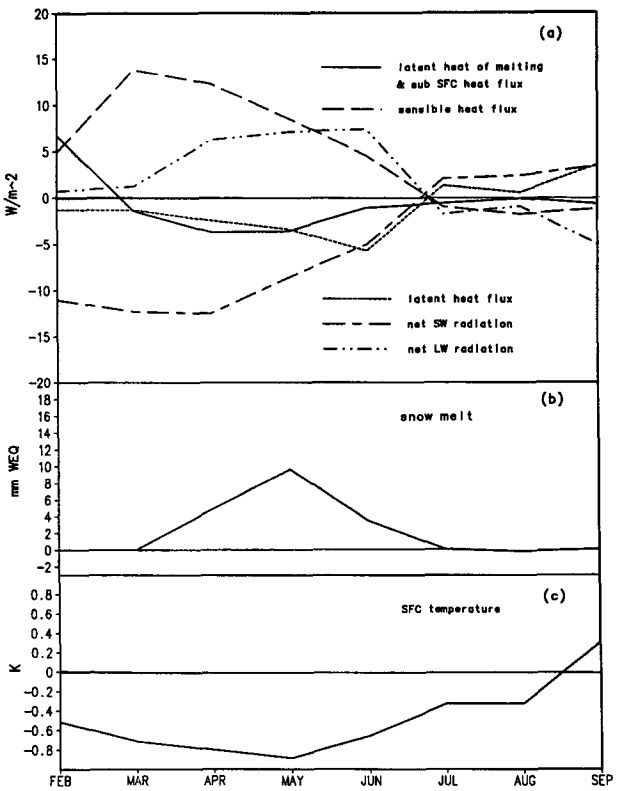

FIG. 8. Seasonal variation of difference (HSE − LSE) in surface heat fluxes, snowmelt, and surface temperature area-weighted average over the region (70°–105°E, 28°–40°N). (a) The difference in surface heat fluxes. (b) The difference in snowmelt. (c) The difference in surface temperature. Tick marks on the abscissa refer to the monthly average (or refer to the middle of the month).

long as the snow is present. The difference in the heat fluxes are close to zero in July when all the snow over the region is melted. Prior to July, the contribution to surface temperature due to shortwave radiation absorbed and the latent heat flux due to evaporation are negative, whereas the sensible heat flux and net longwave radiation emitted from the surface are positive. The shortwave radiation and the sensible heat flux are dominant prior to the establishment of the monsoon in June. From February to April, the difference in the shortwave radiation is ~ 12 W m^{-2} less in HSE compared to that in LSE. This is largely because of the snow albedo effect. After April, a large amount of snow melts in both HSE and in LSE, effectively decreasing the snow extent and the albedo effect. The magnitude of the sensible heat flux difference is about the same as that of the shortwave radiation but of opposite sign. When snow is present on the ground, the surface temperature is colder than without snow. The overlaying air over the colder surface is stable and hence the turbulence transfer process is less effective. From March to July, the snow albedo effect in HSE is compensated by the sensible heat flux. The snow albedo effect dominates only in February. Although snow is a good emitter of longwave radiation, the net longwave radiation in HSE is less than in LSE until July because of lower surface temperature. The latent heat flux difference is very small in February and March. It gradually increases as the snowmelt difference increases. Although the surface temperature is lower in HSE, the availability of snowmelt water dominates the evaporation. The maximum evaporation difference occurs in June when most of the snow is melted. The latent heat of melting and the subsurface heat flux were computed as the residual of the surface energy balance equation. In February the snowmelt difference is zero. The positive sign indicates that subsurface heat flux received at the surface is larger in HSE than in LSE. After March, the snowmelt difference increases and hence the latent heat of melting. The snowmelt water not only increases the soil moisture but also the heat capacity of the soil. The surface temperature in HSE remains colder long after all the snow is melted because of the large heat capacity of the wetter surface.

In summary, the surface temperatures over the region are colder in HSE than in LSE because of the snow albedo effect in February, energy used in melting excessive snow in April through June, and because of the greater heat capacity of wetter soil from July through mid-August.

To see how the atmospheric heating is affected by the excessive snow cover in HSE, we present the seasonal variation of the difference (HSE − LSE) in diabatic heating components vertically averaged from surface to 200 mb and areally averaged over the same region (70°–105°E, 28°–40°N) in Fig. 9. While all the results presented here are based on the ensemble average of four runs, the results in Fig. 9 are based only

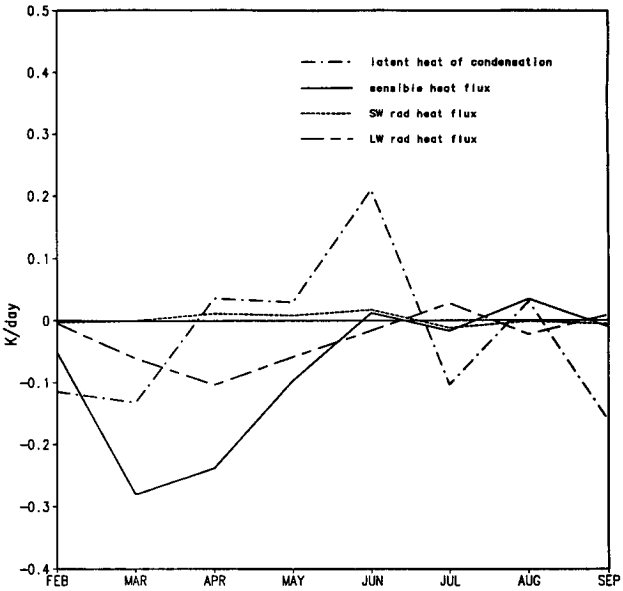

FIG. 9. Seasonal variation of difference (HSE − LSE) in diabatic heating rates in the atmospheric column (from surface to 200 mb) vertically and area-weighted average over the region (70°–105°E, 28°–40°N). The diabatic heating rates are due to shortwave radiation, longwave radiation, sensible heat flux, and latent heat flux. Tick marks on the abscissa refer to the monthly average (or refer to the middle of the month).

on the ensemble average of three runs. In the run with initial conditions of 2 February, the data for these heating components were not saved. The solar heating difference in the two experiments is negligible. The longwave heating is less in HSE than in LSE from February to June but the magnitude of the difference is small. Heating due to the latent heat of condensation is less in HSE than in LSE in February, March, July, and September. Only in June does the heating in HSE exceed that of LSE. For other months, the difference is very small. Heating due to sensible heat flux is smaller in HSE than in LSE from February to June and the magnitude of the difference is large compared to the other heating processes. The difference is lowest (~ -0.3 K day^{-1}) in March when the surface heat flux converging toward the earth's surface is a maximum. In other words, heat lost by the surface due to sensible heat flux in HSE was minimal. Hence the atmospheric column over the region is colder in HSE because of less sensible heat flux received from the earth's surface.

We have seen from Fig. 8c that the surface temperature averaged over the region (28°–40°N, 70°–105°E) is colder in HSE than in LSE from February through August and it is coldest in May. Figure 10 shows how this cooling in May is distributed in the vertical and along 60°–120°E averaged over the latitude belt 28°–40°N. The cooling is throughout the troposphere but restricted to the plateau region.

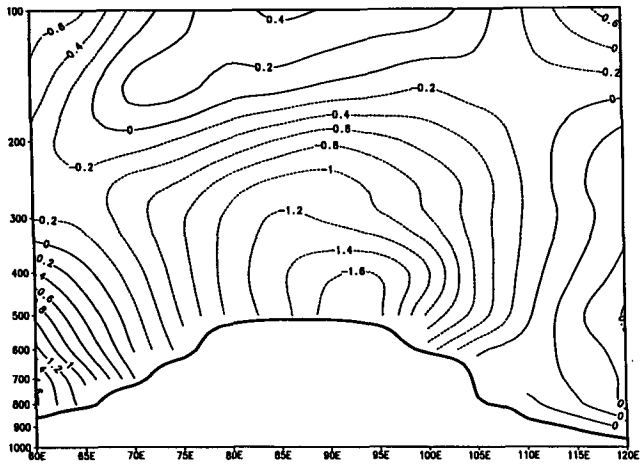

FIG. 10. Vertical cross section of May temperature difference (HSE − LSE) along 60°–120°E area-weighted average over the latitude belt 28°–40°N. Bold line shows the profile of mean orography in the model along 60°–120°E averaged over the latitude belt 28°–40°N. Contour interval is 0.2 K.

There is warming to the east and to the west of the plateau. The maximum cooling of 1.6°K near 95°E coincides with the region of excessive initial snow cover in HSE (see Fig. 4c).

b. Premonsoon circulations

The monsoon circulations are established at the time of the onset. The climatological onset date at the southern tip of the Indian peninsula is 1 June with a standard deviation of eight days (Soman and Kumar 1993). However, some features of the monsoon circulation appear in May (Krishnamurti 1985).

We have seen in Fig. 7 that the 500-mb mean May temperature difference (HSE − LSE) is negative over a broad region surrounding Tibet. This reduces the north–south temperature gradient between the equator and 30°N over the Indian subcontinent. The impact of the reduced temperature gradient is to reduce the intensity of the circulation. One of the important features of the monsoon circulation is the establishment of the monsoon trough along the Ganges River from the northwest to the southeast. The intensity of the monsoon is proportional to the depth of the trough. The May sea level pressure in LSE shows the establishment of the monsoon trough (Fig. 11a). Figure 11b shows the difference (HSE − LSE) in sea level pressure. The positive values over India indicate that the monsoon trough is relatively shallow in HSE. Another feature of the monsoon circulation is that the lower tropospheric easterly flow over the Indian Ocean associated with the Mascarene High crosses the equator along the Somali Jet and then turns eastward to cross the Arabian Sea and the Indian peninsula. The flow then continues northeastward along the monsoon trough. These features in LSE are seen in Fig. 12a. The anomalous easterlies in Fig. 12b suggest that the westerlies over the southern part of the peninsula are weaker in HSE. At the time of the establishment of the monsoon circulation, the upper tropospheric subtropical westerly jet shifts northward. The tropical easterly jet strengthens and moves northward. The high from the South China Sea moves northwestward. These features are well simulated in LSE (Fig. 13a). Similar features were present in HSE but the easterly jet was weaker as indicated by westerly anomaly near the equator in Fig. 13b and the westerly

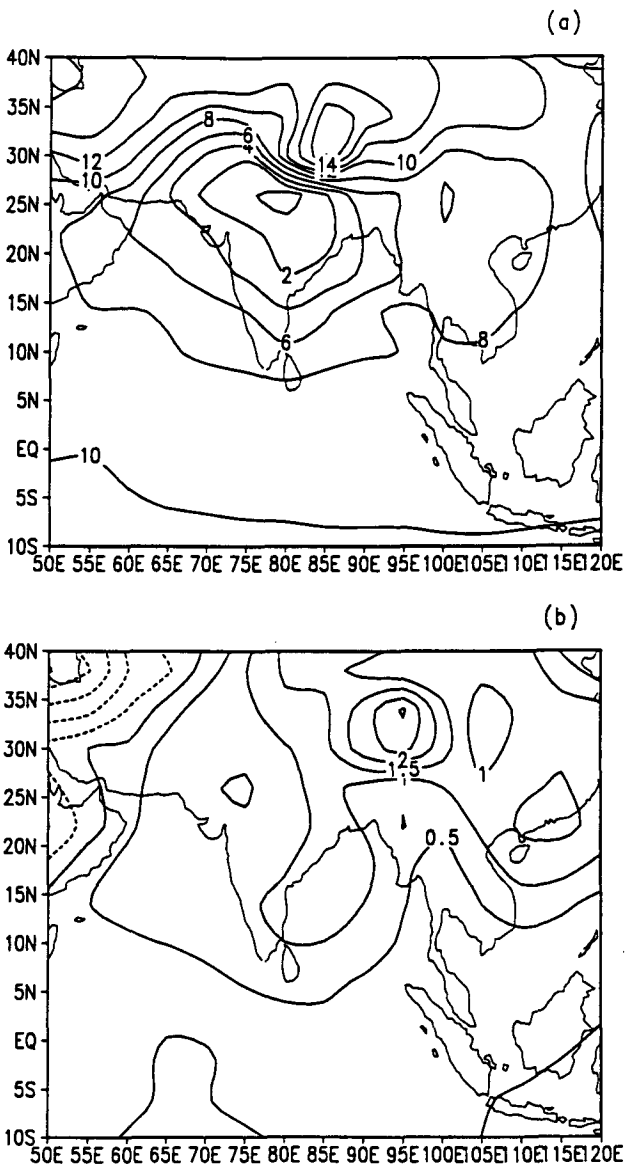

FIG. 11. Regional distribution of May sea level pressure departure from 1000 mb. (a) For LSE, contour interval is 2 mb. (b) For (HSE − LSE) difference, contour interval is 0.5 mb.

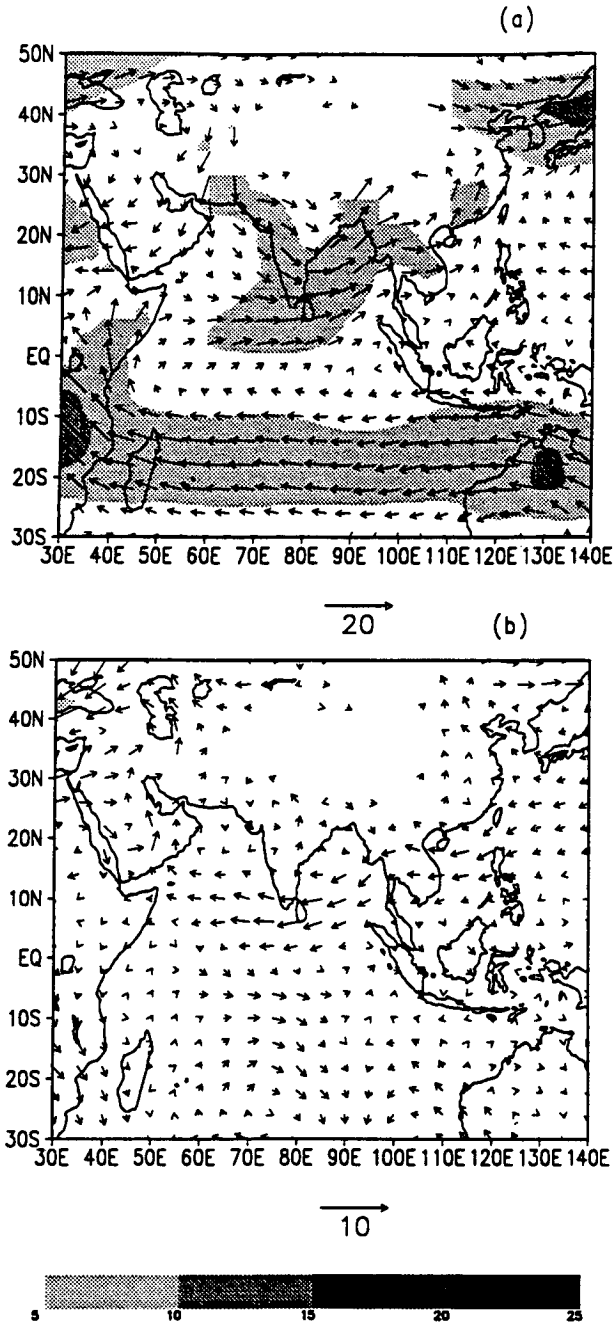

FIG. 12. Regional distribution of May 850-mb wind (m s^{-1}). (a) For LSE. (b) For (HSE − LSE) difference. Lower scale of gray shade shows magnitude of wind.

jet did not move as far north in LSE as shown by westerly anomaly near 20°N over the peninsula. In May, heavy rains occur in southeast China, Assam, Burma, and in the Bay of Bengal. These features are well simulated in LSE (Fig. 14a). A similar pattern was in HSE but the intensity of the rains were much weaker with an almost 50% decrease along the axis of heavy rain (Fig. 14b).

c. *Monsoon circulation*

There is empirical evidence that the excess of snow cover over the Himalayan region delays the onset of the monsoon (Dey and Kathuria 1986) and extends the withdrawal period (Dey et al. 1985). Similar characteristics were found in these simulations.

The monsoon onset, referred to as "monsoon burst," occurs when the level of energetics of the circulation

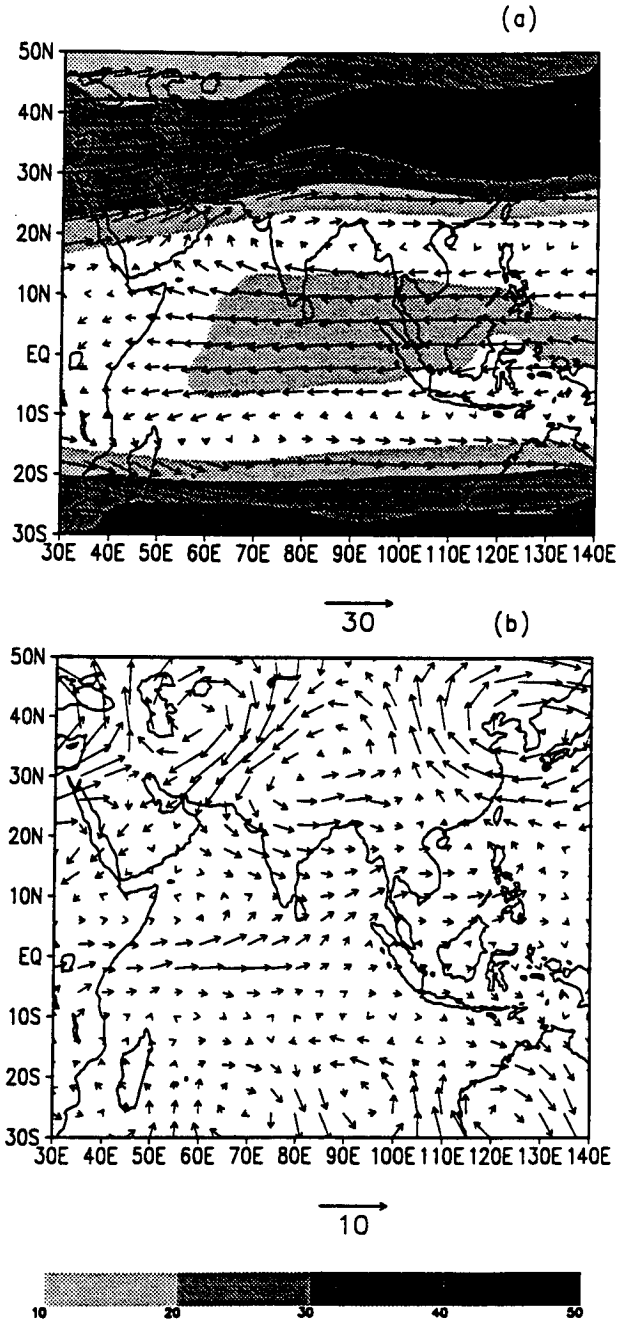

FIG. 13. Same as Fig. 12 except for 200-mb wind.

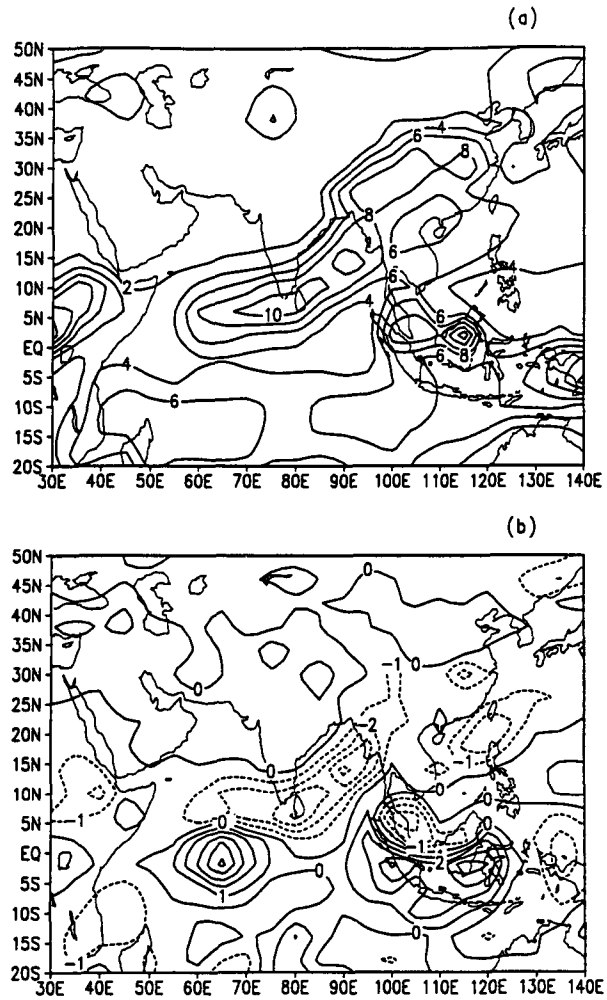

FIG. 14. Regional distribution of May precipitation rate. (a) For LSE, contour interval is 2 mm day^{-1}. (b) For (HSE − LSE) difference, contour interval is 1 mm day^{-1}.

over Indian region increases several-fold in a very short period of time. As the seasonal insolation propagates northward from the March equinox to the June solstice, the latitude of the warmest midtropospheric temperature shifts northward. The seasonal variation of the latitude of maximum 500-mb temperature averaged over the sector (70°–100°E) for the two experiments is shown in Fig. 15. In both of the experiments the latitude shifts from 5° to 10°N latitude in about two months from March to May. Then it shifts from 15° to 30°N in three weeks from the middle of May to the first week of June. It remains near 30°N until the beginning of September and then moves southward. The main difference in the two curves is that in HSE there is a delay of about 10 days to reach 30°N compared to that in LSE. If we associate the latitude of maximum temperature movement southward to the withdrawal period, we find there is a delay in the withdrawal in HSE in agreement with the observations.

Krishnamurti and Ramanathan (1982) investigated the role of differential heating between the land and the ocean on the sudden increase in the kinetic energy (KE) level of the monsoon circulation at the time of the monsoon onset. During the premonsoon period, the midtroposphere is warmed over the Tibetan Plateau due to sensible heat flux. Also during that period, heavy rains east of Tibet, Assam, and Burma and thunderstorms over the Indian peninsula warm the midtroposphere by the latent heat of condensation. As the season progresses, midtropospheric warm air over the Indian region is heated continuously by the latent heat of condensation associated with the monsoon rains. Heating warm air generates available potential energy. The available potential energy is then converted to the kinetic energy (KE) of irrotational motion (K_χ) through buoyancy forces. The KE of irrotational motion in turn is converted to KE of rotational motion (K_ψ).

There are four terms that contribute to the conversion of KE of irrotational motion to the rotational motion $C(K_\chi, K_\psi)$. Krishnamurti and Ramanathan (1982) have shown that the most dominant term in $C(K_\chi, K_\psi)$ is $\overline{f\nabla\psi\cdot\nabla\chi}$, where f is the Coriolis parameter, ψ is the streamfunction, χ is the velocity potential, and the bar represents the regional average. At the time of the monsoon onset, the KE level over the Indian region increases throughout the troposphere. However, the largest increase occurs close to the earth's surface. We have computed the seasonal variations of $C(K_\chi, K_\psi)$, K_χ, and K_ψ areally averaged over the region (6°–26°N, 70°–100°E) and from the surface to 850 mb. The variations of conversion rate from the KE of irrotational motion to the KE of rotational motion is shown in Fig. 16. The conversion rate dramatically increases from the middle of May, reaches a maximum in the beginning of July, and then decreases. The difference between the two experiments is that in HSE

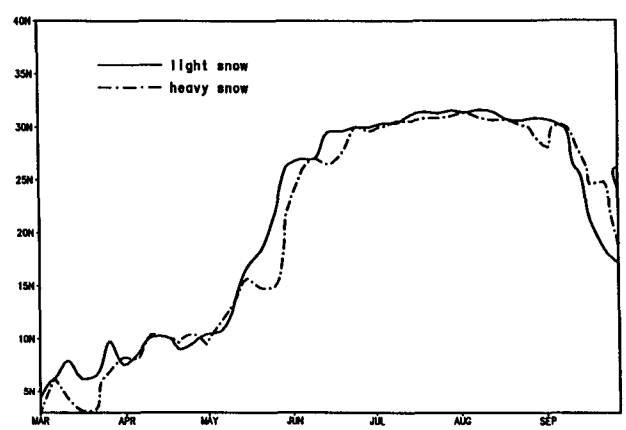

FIG. 15. Seasonal variation of latitude of maximum 500-mb temperature averaged over the sector (70°–100°E) for LSE and HSE.

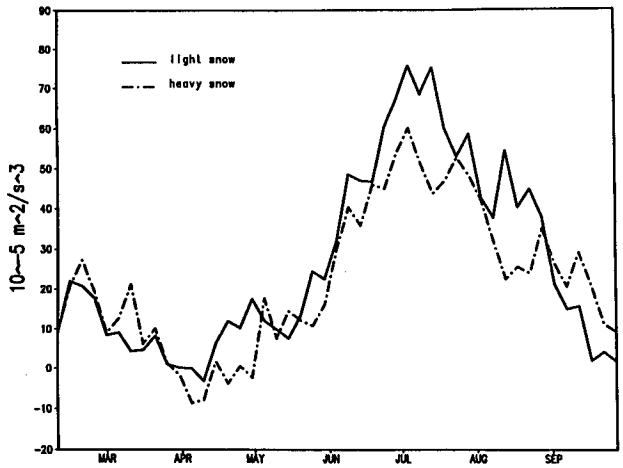

FIG. 16. Seasonal variation of conversion from KE of irrotational motion to KE of rotational motion averaged from 850 mb to surface and over the region (70°–100°E, 6°–26°N) for LSE and HSE. Units: 10^{-5} m^2 s^{-3} same as in Krishnamurti (1985). Tick marks on the abscissa refer to the beginning of the month.

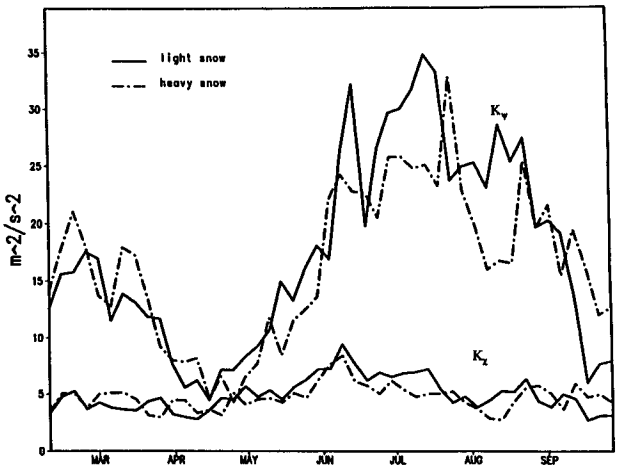

FIG. 17. Seasonal variation of KE of rotational and irrotational motion averaged from surface to 850 mb and over the region (70°–100°E, 6°–26°N) for LSE and HSE. Units: m^2 s^{-2}. Tick marks on the abscissa refer to the beginning of the month.

the rate of conversion is lower than that in LSE but it is slightly higher during the monsoon withdrawal period in September. The variations of the KE of rotational and irrotational motion is shown in Fig. 17. The energy level of both the components is almost the same during April. During the monsoon season, the KE of rotational motion is about four times as large as the KE of irrotational motion. The energy levels are higher in LSE than in HSE but slightly less during the monsoon withdrawal. These temporal characteristics of KE in the model agree well with observations (Krishnamurti and Ramanathan 1982; Webster and Yang 1992).

We have seen that HSE circulations are weaker than those of LSE. However, the empirical evidence is that the summer monsoon precipitation for JJAS over India is less during the years of heavy snow cover. Figure 18a shows the JJAS precipitation pattern for LSE. The rainfall pattern resembles well the climatological rainfall pattern over the Indian region—a large center of maximum rainfall in the Bay of Bengal, Bangladesh, and Assam. There is a relatively smaller maximum on the west coast of India. In the climatology, the rainfall on the west coast is equally strong. The precipitation rate areally averaged over the region (10°–30°N, 60°–100°E) is 7.4 mm day^{-1} or about 900 mm for four months. This is comparable to the observed climatological rainfall over India of 850 mm (Mooley and Shukla 1987). In HSE, the average precipitation rate is 7 mm day^{-1} or 850 mm for four months. The standard deviation computed from the four runs is ~0.4 mm day^{-1} in both of the experiments. The observed standard deviation is ~0.8 mm day^{-1} (Mooley and Shukla 1987). The standard deviation in the experiment is considered only due to internal dynamics, whereas in the observations, it is also due to interannual

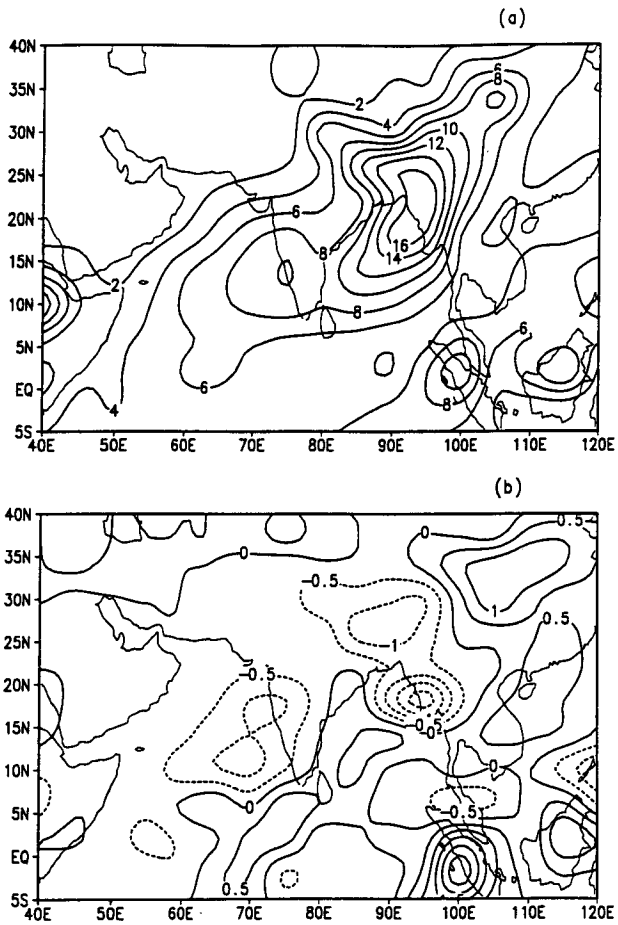

FIG. 18. Regional distribution of JJAS precipitation rate. (a) For LSE, contour interval is 2 mm day^{-1}. (b) For (HSE − LSE) difference, contour interval is 0.5 mm day^{-1}.

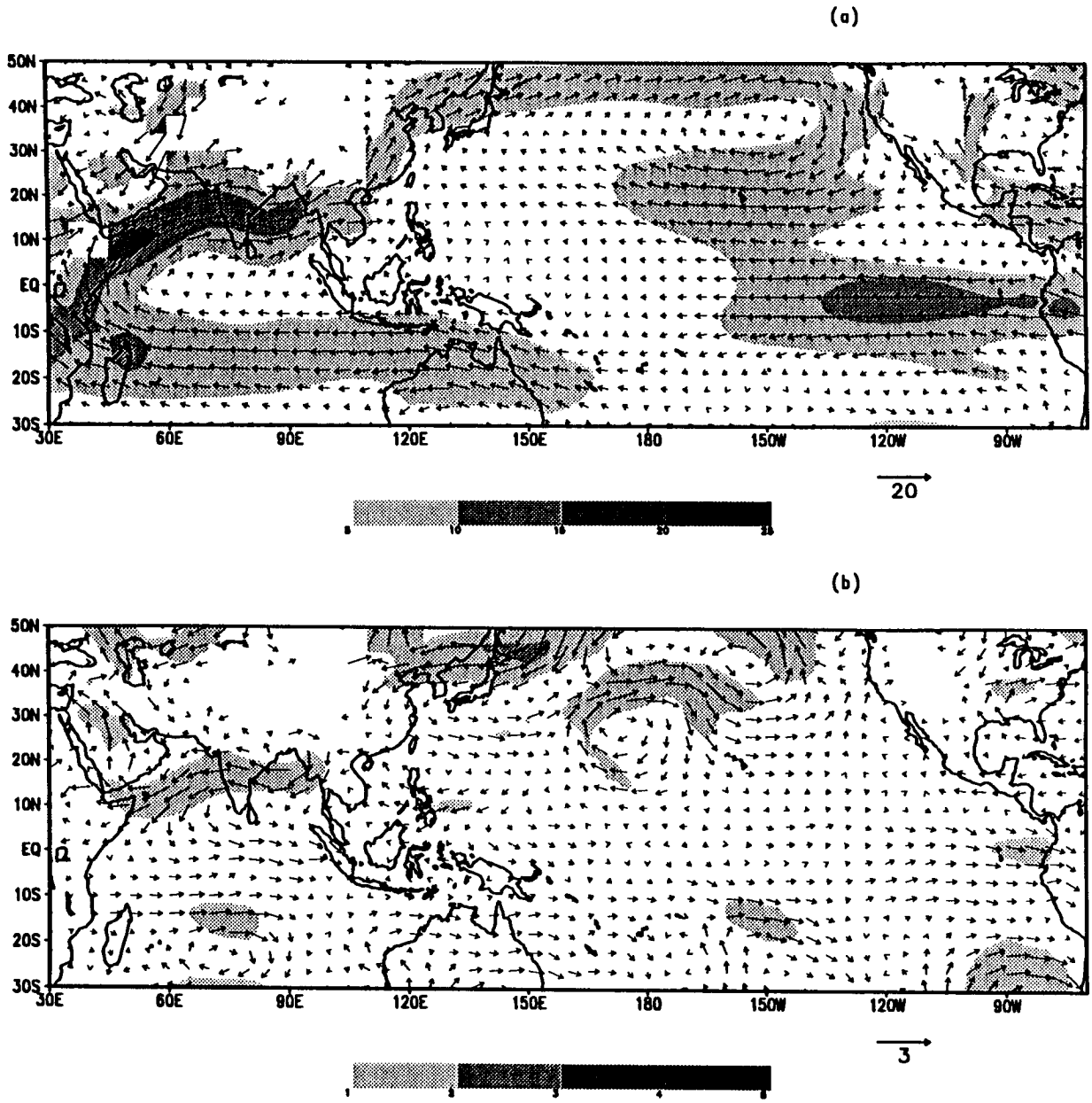

FIG. 19. Regional distribution of JJA 850-mb wind (m s^{-1}). (a) For LSE. (b) For (HSE − LSE) difference. Lower scale of gray shade shows magnitude of wind.

variability in global boundary conditions. The difference in the rainfall pattern in Fig. 18b shows the decrease in the rainfall at the centers of maximum precipitation. The magnitude of the difference is about one standard deviation, that is, 0.4 mm day^{-1}: Barnett et al. (1989) present composite maps of Indian rainfall departures for years of heavy and light Eurasian snow cover (see Fig. 12 in Barnett et al.). These figures show, in both cases, a maximum departure of half a standard deviation. The results in Fig. 18b compare favorably with their composite maps.

The influence of the Eurasian snow cover is not only over the Indian region but also over the rest of the globe. Here we present the influence on the lower tropospheric circulation over the Indian region and the Pacific Ocean (Fig. 19a). The 850-mb wind circulation shows the typical easterlies in the Indian Ocean crossing the equator along the Somali Jet then turning to westerly flow over the Indian peninsula and then to southwesterly flow around the monsoon trough. Over the equatorial Pacific Ocean, the trades are of magnitude ~5–10 m s^{-1}. In the northern Pacific Ocean, relatively

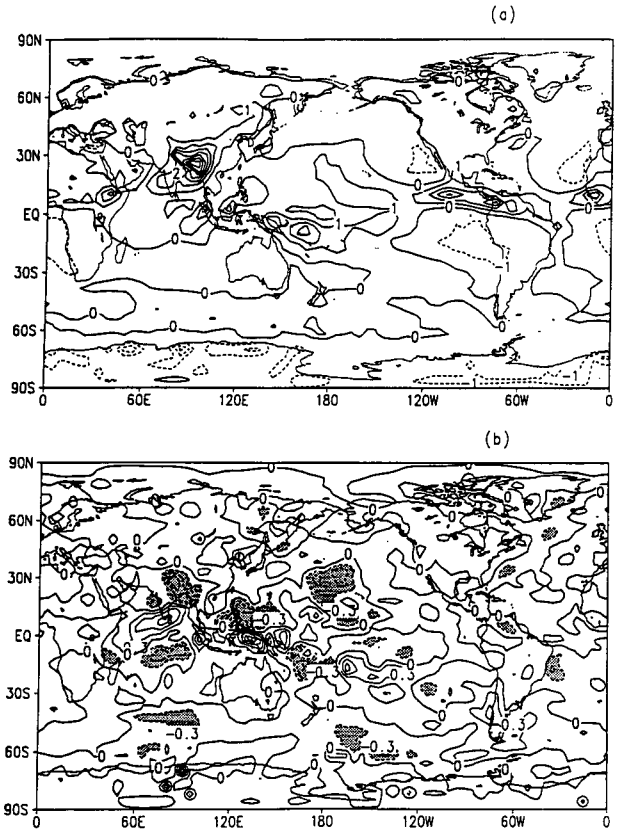

FIG. 20. Global distribution of July vertically averaged diabatic heating rates in the atmosphere. (a) For LSE, contour interval is 1 K day^{-1}. (b) For (HSE − LSE) difference, contour interval is 0.3 K day^{-1}. Shaded region shows negative difference equal to or exceeding 0.3 K day^{-1}.

strong trade winds are associated with the Pacific High, and typical weak trade winds over the warm pool of water in the western Pacific. Figure 19b shows the difference between the two experiments. The circulations are weaker in HSE than in LSE. The anomalous westerlies in the eastern equatorial Pacific Ocean (120°–80°W) indicate weak trade winds in HSE. Similar results were reported in Barnett et al. (1989) and Yasunari (1992). There is also observational evidence that the trade winds in the eastern equatorial Pacific Ocean are strong (weak) when monsoon circulations are strong (weak) (Meehl 1987; Webster and Yang 1992). Weak trade winds are precursors to El Niño (Rasmusson and Carpenter 1982). It is possible that excessive winter/spring snow cover over Eurasia alters El Niño period.

To examine the effect of Eurasian snow cover on the global distribution of heating, we present Fig. 20. Figure 20a shows the July mean vertically averaged global distribution of heating in LSE. The region of maximum heating rate (>2°K day^{-1}) is over the Indian monsoon region. The other heating regions are along the SPCZ and over the central American and central African parts of the ITCZ. The general distribution of heating agrees well with estimated mean heating rates for July derived from observations (Johnson et al. 1987). The regions of cooling in the eastern north and south subtropical Pacific Ocean and in the eastern north and south subtropical Atlantic Ocean also agree well with the results of Johnson et al. (1987). The observed estimates of cooling rates in the southern Indian Ocean, however, are not well simulated. Figure 20b shows the difference (HSE − LSE) in the heating rate. The large regions of negative difference over the tropical belt between 60°E and 120°W seen in this figure suggest that the effect of Eurasian snow cover is not only concentrated over the Indian region but over a much larger region. The effect of Eurasian snow cover on the global distribution of the secondary circulations represented by the velocity potential and the associated divergent wind field at 200 mb is shown in Fig. 21. The mean July global distribution of secondary circulations at 200 mb in LSE is shown in Fig. 21a. The zonal wavenumber one character of the velocity potential agrees well with that estimated from observations (see Fig. 3b in Krishnamurti 1985). The centers of converging winds over the southeastern tropical Pacific Ocean and over northern and southern Africa also agree well with observations. The same is true for the center of diverging winds in the western Pacific Ocean just north of the equator. The global distribution of July mean 200-mb velocity potential in HSE had a similar pattern as in Fig. 21a but its amplitude was smaller. This can be seen in Fig. 21b, which shows the difference (HSE − LSE) in velocity potential and associated divergent winds. The lower magnitude of velocity potential in HSE is consistent with smaller heating rates over the tropical belt between 60°E–120°W seen in Fig. 20b.

4. Summary and concluding remarks

The purpose of this study is to model and simulate the observed evidence that excessive winter/spring Eurasian snow cover reduces the Indian monsoon rainfall the following summer. We have used an improved version of the COLA-GCM (R40, L18) that reproduces the observed Indian monsoon circulation and precipitation patterns.

We have conducted two experiments with the model. The experiments were identical except for initial snow cover over Eurasia. From nine years of *Nimbus-7* SMMR data, we obtained the maximum and minimum snow depth at every gridpoint over Eurasia. In one experiment, we prescribed the maximum snow depth and in the other, minimum snow depth. Four runs were made with initial conditions of four consecutive days to compute ensemble means.

We have shown that the maximum initial snow depth in February reduces JJAS precipitation over India. The excessive snow cover is associated with a weak

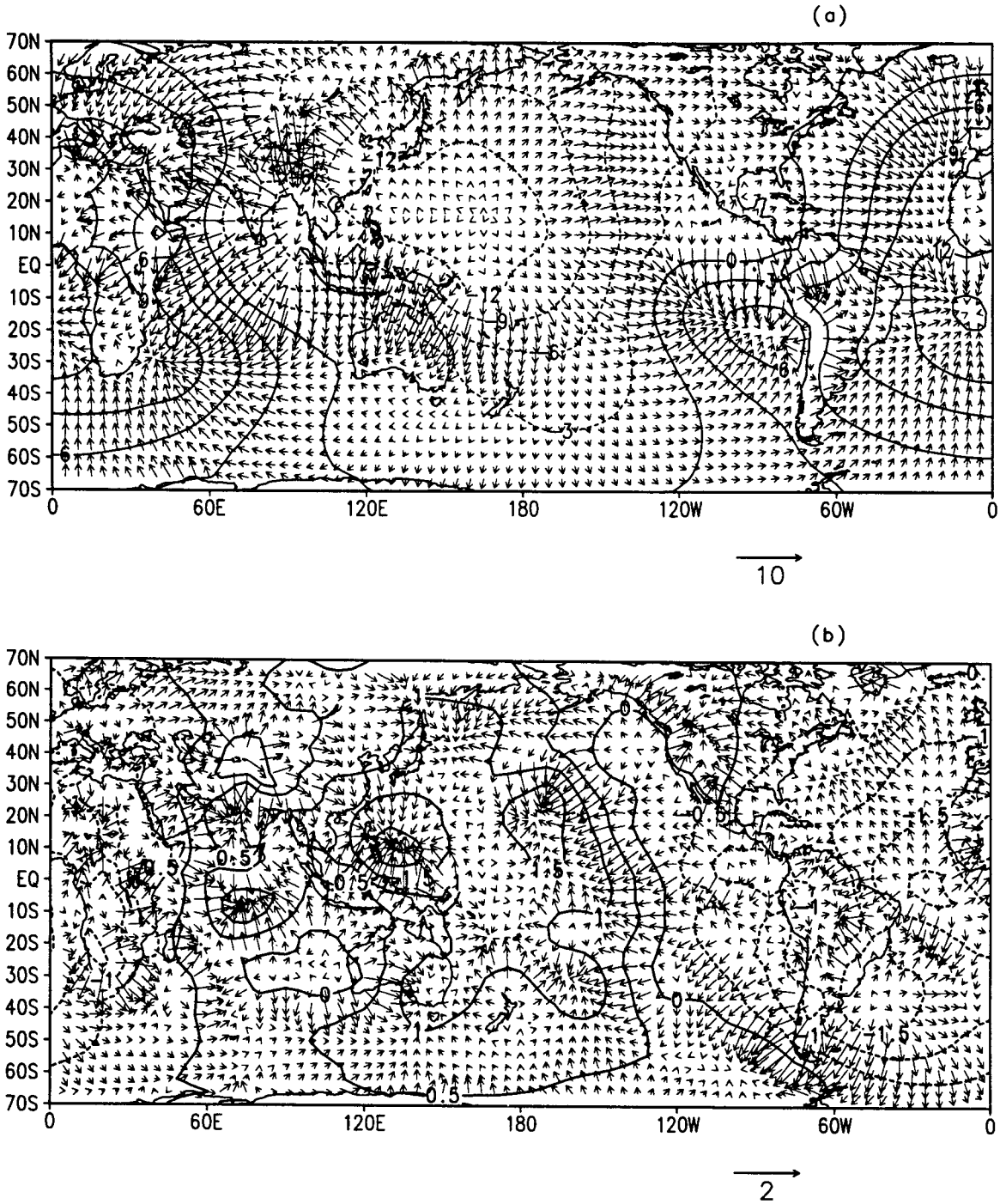

FIG. 21. July 200-mb velocity potential and associated wind vectors of irrotational motion. (a) For LSE. (b) For (HSE − LSE) difference.

monsoon circulation, a delay in the monsoon onset, and a delay in the monsoon withdrawal in agreement with observations.

The weak monsoon is characterized by higher sea level pressure over India, a weaker Somali Jet, weaker lower tropospheric westerlies, and weaker upper tropospheric easterlies.

The weak monsoon circulations are associated with weaker secondary circulations and a smaller magnitude global velocity potential field. The remote response is

to reduce the strength of the trade winds in the equatorial eastern Pacific Ocean.

The reduction of the midtropospheric meridional temperature gradient between the equator and 30°N along the Indian peninsula seems to be responsible for the reduction in the intensity of the monsoon circulation. In the experiment with initial heavy snow cover, the surface temperature over Tibet is reduced largely by the latent heat of melting. The albedo effect, which reduces the solar radiation absorbed at the surface, is canceled by the reduction in the heat loss due to sensible heat flux. Energy lost by the excess evaporation because of the availability of snowmelt water is almost canceled by energy gain by emitting longwave radiation at lower temperatures. When all of the snow is melted, the increase in soil moisture increases the heat capacity of the surface to maintain lower surface temperature during the monsoon season. The tropospheric temperature is lower because of the reduction in the sensible heat flux received from the surface.

The average precipitation difference between the two experiments is 0.4 mm day^{-1}, which is equal to one standard deviation. If we assume that the probability distribution of the average precipitation rate is Gaussian, then the difference is not statistically significant at the conventional level of five percent. We computed the "t" statistic at each grid point. The "t" was significant at five percent level only at the centers of maximum decrease. Yasunari et al. (1991) also had similar results. Barnett et al. (1989) found statistically significant results but the magnitude of the snow anomaly in their experiment in June was almost ten times as large as in the present study. Zwiers's (1993) study was realistic because it was based on model-generated interannual changes of snow cover but the results were not statistically significant.

The limitation of the present study is the prescribed initial snow depth in the two experiments and the short integration time (less than a year). For a realistic experiment, it is necessary to simulate observed changes in the monsoon circulation and precipitation pattern in two years with above and below Eurasian snow cover and near normal surface temperatures in the Indian and Pacific Oceans.

While the model simulates the surface processes fairly accurately, a diagnostic method is used to compute snow accumulation and snow melting. That is, the predicted surface temperature determines the snow accumulation and melting process. For a realistic experiment, it is necessary that the model includes a prognostic method for the snow accumulation and melting process. The method should include a snow pack with density varying in the vertical and should consider the balance of mass and energy within the snow pack as well as at the top and bottom of the snow pack (Loth et al. 1993).

In the present study, we have not attempted to determine whether the snow anomaly on the continental scale or the snow anomaly over a limited region (e.g., the Tibetan Plateau) was the dominating factor. Identifying such a dependence is crucial considering the usefulness of this relation for the long-range forecast of the Indian summer monsoon and the economical constraints of monitoring snow depth.

Acknowledgments. We thank anonymous reviewers for their constructive comments for improvement of the original draft of this paper. We are grateful to Dr. James Kinter for carefully reading the revised manuscript, making editorial corrections to improve the text, and giving valuable suggestions.

This research was supported by the Climate Dynamics Program of the NSF under Grants ATM-9114318 and ATM-9019296. Snow depth data for the study were provided by the Pilot Land Data System at NASA Goddard Space Flight Center (GSFC) in Greenbelt, Maryland. Most of the computations for this study were made on the CRAY Y-MP at NASA GSFC. Partial computer support was provided by the Scientific Computing Division at NCAR which is supported by the NSF. The first author (ADV) would like to acknowledge the support of the NOAA Indo-U.S. Climate Research Program for his visit to New Delhi to present preliminary results of this study in the MONEG meeting in 12–14 January 1993. The authors are indebted to Claire Selleck for her help in preparing the manuscript.

REFERENCES

Anthes, R. A., 1977: Hurricane model experiments with a new cumulus parameterization scheme. *Mon. Wea. Rev.*, **105,** 287–300.

Barnett, T. P., L. Dümenil, V. Schlese, E. Roeckner, and M. Latif, 1989: The effect of Eurasian snow cover on regional and global climate variations. *J. Atmos. Sci.*, **46,** 661–685.

Blanford, H. F., 1884: On the connection of Himalayan snowfall with dry winds and seasons of drought in India. *Proc. Roy. Soc. London,* **37,** 3–22.

Chang, A. T. C., J. L. Foster, and D. K. Hall, 1987: *NIMBUS-7* SMMR derived global snow cover parameters. *Ann. Glaciol.*, **9,** 34–44.

Charney, J. G., and J. Shukla, 1981: Predictability of monsoons. *Monsoon Dynamics,* Sir J. Lighthill and R. P. Pearce, Eds., Cambridge University Press, 99–109.

Dey, B., and O. S. R. U. Bhanu Kumar, 1982: An apparent relationship between Eurasian snow cover and the advanced period of the Indian summer monsoon. *J. Appl. Meteor.*, **21,** 1929–1932.

——, and ——, 1983: Himalayan winter snow cover area and summer monsoon rainfall over India. *J. Geophys. Res.*, **88,** 5471–5474.

——, and S. N. Kathuria, 1986: Himalayan snow cover area and onset of summer monsoon over Kerala, India. *Mausam,* **37,** 193–196.

——, ——, and O. B. Kumar, 1985: Himalayan summer snow cover and withdrawal of the Indian summer monsoon. *J. Appl. Meteor.*, **24,** 865–868.

Dickson, R. R., 1984: Eurasian snow cover versus Indian monsoon rainfall—an extension of the Hahn-Shukla results. *J. Climate Appl. Meteor.*, **23,** 171–173.

Dorman, J. L., and P. J. Sellers, 1989: A global climatology of albedo, roughness length and stomatal resistance for atmospheric general

circulation models as represented by the Simple Biosphere Model (SiB). *J. Appl. Meteor.*, **28,** 833–855.

Fennessy, M. J., J. L. Kinter III, B. Kirtman, L. Marx, S. Nigam, E. Schneider, J. Shukla, D. Straus, A. Vernekar, Y. Xue, and J. Zhou, 1994: The simulated Indian monsoon: A GCM sensitivity study. *J. Climate,* **7,** 33–43.

Flohn, H., 1950: Studien zur allgemeinen Zirkulation der Atmosphäre III. *Ber. Deutsch. Wetterdienstes,* **18,** 34–50.

——, 1960: Recent investigations on the mechanism of "summer monsoon" of southern and eastern Asia. *Proc. Symp. Monsoon of the World,* Hind Union Press, 75–88.

Gao, Y.-X., M.-C. Tang, S.-W. Luo, Z.-B. Shen, and C. Li, 1981: Some aspects of recent research on Qinghai-Xizang Plateau meteorology. *Bull. Amer. Meteor. Soc.,* **62,** 31–35.

Hahn, D. J., and S. Manabe, 1975: The role of mountains in the south Asian monsoon circulation. *J. Atmos. Sci.,* **32,** 1515–1541.

——, and J. Shukla, 1976: An apparent relationship between Eurasian snow cover and Indian monsoon rainfall. *J. Atmos. Sci.,* **33,** 2461–2462.

Harshvardhan, R. Davies, D. A. Randall, and T. G. Corsetti, 1987: A fast radiation parameterization for general circulation models. *J. Geophys. Res.,* **92,** 1009–1016.

He, H., J. W. McGinnis, Z. Song, and M. Yanai, 1987: Onset of the Asian summer monsoon in 1979 and the effect of the Tibetan Plateau. *Mon. Wea. Rev.,* **115,** 1966–1995.

Helfand, H. M., J. C. Jusem, J. Pfaendtner, J. Tenenbaum, and E. Kalnay, 1987: The effect of a gravity wave drag parameterization on GLA four order GCM forecasts. *NWP Symp. on Short and Medium-Range Numerical Weather Prediction,* Tokyo, Japan, WMO/IUGG.

Hou, Y.-T., 1990: Cloud-radiation-dynamic interaction. Ph.D. dissertation, University of Maryland, College Park, 205 pp.

Janowiak, J. E., and P. A. Arkin, 1991: Rainfall variations in the tropics during 1986–1989, as estimated from observations of cloud-top temperature. *J. Geophys. Res.,* **96,** 3359–3373.

Johnson, D. R., M. Yanai, and T. K. Schaack, 1987: Global and regional distribution of atmospheric heat sources and sinks during GWE. *Monsoon Meteorology,* C. P. Chang and T. N. Krishnamurti Eds., Oxford University Press, 271–297.

Kirtman, B., A. Vernekar, D. Dewitt, and J. Zhou, 1993: Impact of orographic gravity wave drag on extended-range forecasts with the COLA-GCM. *Atmosfera,* **6,** 3–24.

Krishnamurti, T. N., 1985: Summer monsoon experiment—a review. *Mon. Wea. Rev.,* **113,** 1590–1626.

——, and Y. Ramanathan, 1982: Sensitivity of the monsoon onset to differential heating. *J. Atmos. Sci.,* **39,** 1290–1306.

Kuo, H. L., 1965: On the formation and intensification of tropical cyclones through latent heat release by cumulus convection. *J. Atmos. Sci.,* **22,** 40–63.

——, and Y.-F. Qian, 1981: Influence of the Tibetan Plateau on cumulative and diurnal changes of weather and climate in summer. *Mon. Wea. Rev.,* **109,** 2337–2356.

——, and ——, 1982: Numerical simulation of the development of mean monsoon circulation in July. *Mon. Wea. Rev.,* **110,** 1879–1897.

Lacis, A. A., and J. E. Hansen, 1974: A parameterization of the absorption of solar radiation in the earth's atmosphere. *J. Atmos. Sci.,* **31,** 118–133.

Loth, B., H.-F. Graf, and J. M. Oberhuber, 1993: Snow cover model for global climate simulations. *J. Geophys. Res.,* **98,** 10 451–10 464.

Luo, H., and M. Yanai, 1983: The large-scale circulation and heat sources over the Tibetan Plateau and surrounding areas during the early summer of 1979. Part I: Precipitation and kinematic analysis. *Mon. Wea. Rev.,* **111,** 922–944.

Matson, M., C. F. Ropelewski, and M. S. Varnadore, 1986: An atlas of satellite-derived Northern Hemisphere snow cover frequency. NOAA Atlas, U.S. Govt. Printing Office, 1986-151-384, 75 pp. [Available from NOAA/NESDIS (E/RA22), 5200 Auth Road, Washington, D.C. 20233.]

Meehl, G. A., 1987: The annual cycle and interannual variability in the tropical Pacific and Indian Ocean region. *Mon. Wea. Rev.,* **115,** 27–50.

Mellor, G. L., and T. Yamada, 1982: Development of a turbulence closure model for geophysical fluid problems. *Rev. Geophys. Space Phys.,* **20,** 851–875.

Mintz, Y., and Y. V. Serafini, 1984: Global fields of monthly normal soil moisture as derived from observed precipitation and estimated potential evaporation. *Land Surface Influences on Weather and Climates.* NASA-CR-173575, 182 pp.

Mooley, D. A., and J. Shukla, 1987: Variability and forecasting of the summer monsoon rainfall over India. *Monsoon Meteorology,* C. P. Chang and T. N. Krishnamurti Eds., Oxford University Press, 26–59.

Nitta, T., 1983: Observational study of heat sources over the eastern Tibetan Plateau during the summer monsoon. *J. Meteor. Soc. Japan,* **61,** 590–605.

Palmer, T. N., G. J. Shutts, and R. Swinbank, 1986: Alleviation of a systematic westerly bias in general circulation and numerical weather prediction models through an orographic gravity wave parameterization. *Quart. J. Roy. Meteor. Soc.,* **112,** 1001–1039.

Peixoto, J. P., and A. H. Oort, 1992: *Physics of Climate.* American Institute of Physics, 520 pp.

Pierrehumbert, R. T., 1987: An essay on the parameterization of orographic gravity wave drag. Geophysical Fluid Dynamics Laboratory/NOAA/Princeton University, 32 pp. [Available from GFDL/NOAA, Princeton University, Princeton, NJ 08542.]

Rasmusson, E. M., and T. H. Carpenter, 1982: Variation in tropical sea surface temperature and surface wind field associated with Southern Oscillation/El Niño. *Mon. Wea. Rev.,* **110,** 354–384.

Reynolds, R. W., 1988: A real-time global sea surface temperature analysis. *J. Climate,* **1,** 75–86.

Riehl, H., 1959: On production of kinetic energy from condensation heating. *The Atmosphere and the Sea in Motion,* The Rossby Memorial Volume, Rockefeller Institute Press, 381–399.

Schutz, C., and L. B. Bregman, 1988: Global annual snow accumulation by months. Rand Note N-2687-RC, 85 pp. [Available from Rand Corporation, 1200 Main Street, Santa Monica, CA 90406.]

Sellers, P. J., Y. Mintz, Y. C. Sud, and A. Dalcher, 1986: A simple biosphere model for use within general circulation models. *J. Atmos. Sci.,* **43,** 505–531.

Shukla, J., 1987: Interannual variability of monsoons. *Monsoons,* Fein and Stephens, Eds., A. Wiley-Interscience, 399–464.

Slingo, J. M., 1980: A cloud parameterization scheme derived from GATE data for use with a numerical model. *Quart. J. Roy. Meteor. Soc.,* **106,** 747–770.

——, 1987: The development and verification of a cloud prediction scheme for ECMRWF model. *Quart. J. Roy. Meteor. Soc.,* **113,** 899–927.

Soman, M. K., and K. Krisna Kumar, 1993: Space-time evolution of meteorological features associated with the onset of Indian summer monsoon. *Mon. Wea. Rev.,* **121,** 1177–1194.

Spencer, R., 1993: Global oceanic precipitation from MSU during 1979–91 and comparisons to other climatologies. *J. Climate,* **6,** 1301–1326.

Tiedtke, M., 1984: The effect of penetrative cumulus convection on large scale flow in a general circulation model. *Beitr. Phys. Atmos.,* **57,** 216–239.

Vernekar, A., B. Kirtman, J. Zhou, and D. Dewitt, 1992: Orographic gravity wave drag effects on medium-range forecasts with a General Circulation Model. *Physical Processes in Atmospheric Models,* D. R. Sikka and S. S. Singh, Eds., 295–307.

Walker, G. T., 1910: On the meteorological evidence for supposed changes of climate in India. *Mem. Indian. Meteor.,* **21,** 1–21.

Webster, P. J., and S. Yang, 1992: Monsoon and ENSO: Selectively interactive systems. *Quart. J. Roy. Meteor. Soc.,* **118,** 877–926.

Xue, Y., P. J. Sellers, J. Kinter, and J. Shukla, 1991: A simplified biosphere model for global climate studies. *J. Climate,* **4,** 345–364.

Yanai, M., and C. Li, 1994: Mechanism of heating and the boundary layer over the Tibetan Plateau. *Mon. Wea. Rev.,* **122,** 305–323.

——, ——, and Z. Song, 1992: Seasonal heating of the Tibetan Plateau and its effects on the evolution of the Asian summer monsoon. *J. Meteor. Soc. Japan,* **70,** 189–221.

Yang, S., and L. Xu, 1994: Linkage between Eurasian winter snow cover and Chinese summer rainfall: Different from the snow-Indian monsoon connection. *Int. J. Climatol.,* **14,** 739–750.

Yasunari, T., 1992: Role of Monsoon on global climate. *The Global Role of Tropical Rainfall,* J. S. Theon, T. Matsuno, T. Sakata, and N. Fugono, Eds., 129–144.

——, A. Kitoh, and T. Tokioka, 1991: Local and remote responses to excessive snow mass over Eurasia appearing in the northern spring and summer climate—a study with the MRI GCM. *J. Meteor. Soc. Japan,* **69,** 473–487.

Yeh, D.-H., 1981: Some characteristics of the summer circulation over the Qinghai-Xizang (Tibet) Plateau and its neighborhood. *Bull. Amer. Meteor. Soc.,* **62,** 14–19.

Zhou, J., 1993: GCM study of interannual of Indian summer monsoon: The impact of anomalous spring Eurasian snow cover. Ph.D. dissertation, University of Maryland, College Park, 136 pp.

Zwiers, F. W., 1993: Simulation of the Asian summer monsoon with the CCC GCM-1. *J. Climate,* **6,** 470–486.